A solar cycle of upper thermosphere density observations from the EISCAT Svalbard Radar

H. Vickers[1], M. J. Kosch[2,5], E. Sutton[3], L. Bjoland[1], Y. Ogawa[4], and C. La Hoz[1]

[1]Institute for Physics and Technology, University of Tromsø, Tromsø, Norway, [2]South African National Space Agency, Hermanus, South Africa, [3]Air Force Research Laboratory, Kirtland AFB, New Mexico, USA, [4]NIPR, Tokyo, Japan, [5]Lancaster University, Lancaster, UK

Abstract We exploit a recently developed technique, based on ion-neutral coupling, which allows estimations of the upper thermospheric neutral density using measurements of ionospheric plasma parameters made by the European Incoherent Scatter (EISCAT) Svalbard Radar (ESR). The technique is applied to a 13 year long data set of measurements for the purpose of studying and quantifying the effect of solar activity on the upper thermospheric density inside the polar cap. We concentrate on the effect of solar activity at 350 km altitude and find a strong linear correlation between the ESR estimates for the atomic oxygen density and the solar irradiance proxy $F_{10.7}$ index. We use the relationship to isolate variations in the thermospheric density that are present after solar activity influences are removed. Our results show a decrease in the density of a few percent over the 13 year period, which is nevertheless smaller than the uncertainty associated with the decline. We anticipate that the statistical significance of this result will only increase by studying a longer data set. Conjunctions with the CHAMP satellite that show very good agreement is achieved at 350 km especially during low solar activity.

1. Introduction

The thermosphere responds to several different sources of external forcing, which may be linked to atmospheric disturbances from above and below. The response time can vary from hours to days to tens of years. The thermospheric density determines the amount of atmospheric drag experienced by satellites, which in turn affects their trajectories. Determination of how thermospheric properties are influenced by short and long timescale physical processes is therefore of importance for the purpose of predicting satellite paths as well as from a climatological perspective. A number of studies have reported on the effect of solar forcing on the thermospheric density, and it is this driver which this study will focus on. Solar irradiance at extreme ultraviolet (EUV) wavelengths ($\lambda < 120$ nm) is a major heat source for the thermosphere. Its variation over a solar cycle leads to temperature and hence density changes in the upper thermosphere. In situ observations suggest that the thermospheric mass density increase from solar minimum to maximum at 400 km can be up to an order of magnitude [*Emmert and Picone*, 2010]. The low-latitude thermospheric mass density at 400 km exhibits a linear dependence on the $F_{10.7}$ index, which is believed to represent a reliable proxy for solar irradiance. The dependence is observed to be stronger during the daytime than nighttime [*Liu et al.*, 2005; *Müller et al.*, 2009], a characteristic attributed to greater solar EUV input during daytime hours. At high latitudes a poor correlation between $F_{10.7}$ and the total mass density has been reported by *Liu et al.* [2005], although this study was limited to only 1 year of CHAMP data recorded under solar maximum conditions in 2002.

Satellite measurements of the total mass density at midlatitudes have revealed that the global thermosphere is contracting over decade-long timescales [e.g., *Keating et al.*, 2000; *Marcos et al.*, 2005; *Emmert et al.*, 2008]. The rate of decrease in the thermospheric mass density at 400 km is apparently sensitive to the level of solar activity. It is estimated that the rate of contraction ranges from 2% to 5% per decade at solar maximum and minimum, respectively [*Emmert et al.*, 2004, 2008]. The different rates of contraction have been attributed to the different contributions of CO_2 and NO cooling at solar minimum and solar maximum. It is generally understood that cooling due to NO dominates under higher solar activity while CO_2 cooling plays the most significant role during solar minimum. In addition to in situ observations, modeling studies suggest that the

reduction in thermospheric density is typically 1 to 2% per decade at 400 km [*Qian et al.*, 2006]. Long-term increases in CO_2 concentration have resulted in warming of the troposphere and cooling in the middle and upper atmosphere [*Roble*, 1995]. It is thought that this cooling is in part responsible for the long-term contraction of the thermosphere [*Cnossen*, 2012, and references therein].

Much knowledge of the low-latitude and midlatitude thermosphere characteristics, in particular its density, temperature, and composition, has been gained through use of in situ measurements and modeling studies. There is nevertheless still a lack of understanding with regards to how the upper thermospheric density at high latitudes responds to drivers such as solar forcing, geomagnetic activity, and secular changes, particularly inside the polar cap. Relatively few studies of the thermospheric density have been made using ground-based instrumentation. Earlier attempts of this kind for the high-latitude case are documented in the literature [*Winser et al.*, 1988; *Mikhailov and Lilensten*, 2004; *Blelly et al.*, 2010]. These results have mostly been based on a small number of case studies.

More recent attempts to study the upper thermospheric density inside the polar cap have used a near-continuous database of measurements made by the European Incoherent Scatter (EISCAT) Svalbard Radar [*Wannberg et al.*, 1997] during the international polar year (IPY) which took place from March 2007 to February 2008. This was carried out by means of a novel technique that exploits ion-neutral coupling in the ion momentum balance equation [*Vickers et al.*, 2013]. The method was developed through earlier case study investigations using artificial heating experiments at EISCAT [*Kosch et al.*, 2010] and passive experiments at Poker Flat [*Anderson et al.*, 2012]. In essence, the ion momentum equation is simplified for field-aligned ion motion and quiet geomagnetic conditions ($Kp \leq 2$). Measurements of the ionospheric plasma parameters by incoherent scatter radar are used to derive estimates of the ion-neutral collision frequency, which converts directly into an atomic oxygen density at altitudes between ~250 and 400 km where this is the dominant constituent. The estimates agreed very well with the NRLMSISE-00 empirical neutral atmosphere model [*Picone et al.*, 2002] at an altitude of 350 km. Case study comparisons with in situ density measurements made by the Challenging Minisatellite Payload (CHAMP) satellite [*Reigber et al.*, 2002] also revealed that the estimates compared well with the satellite drag observations that had been normalized to 350 km.

Based on the successful statistical study results of the IPY data set, we now extend the use of the technique to a longer data set spanning more than a whole solar cycle at the European Incoherent Scatter (ESR), beginning from mid-2000 to the end of 2012. This accounts for most of the available data from the 42 m field-aligned dish of the ESR. The objective of the present work is to investigate the degree to which solar activity controls the upper thermospheric density above the ESR. The results of this study contribute to the current knowledge about the role of solar activity and underlying long-term trends in the upper thermosphere, in particular within the polar cap where thermospheric properties are less widely reported. Similar to the earlier work reported in *Vickers et al.* [2013], we endeavor to clarify whether the estimates derived using this ground-based radar technique are consistent with in situ measurements by employing estimates of the total mass density derived from atmospheric drag measurements made by the CHAMP satellite.

In the following section, we outline briefly the instrumentation which was used to provide the data used in the study and how we reduced the ESR database. In section 3 we present the results of our analysis and discuss their significance in section 4. We conclude the findings of the work in section 5.

2. Instrumentation and Data Selection

2.1. EISCAT Svalbard Radar

Experiments with the EISCAT Svalbard Radar (78°09′N, 16°01′E) using the 32 m steerable antenna started in 1996, but operations with the fixed 42 m antenna did not begin until 2000. For this study we analyze only raw data recorded on the 42 m field-aligned antenna. This is necessary since the method for estimating the atomic oxygen density is based on the ion momentum equation simplified for field-aligned motion.

We have obtained data via the web-based EISCAT database from experiments carried out between mid-2000 and the end of 2012. Data were only downloaded where there was more than an hour of experimental data available. Throughout the 13 year period under study, raw data were recorded at four different time resolutions of 3.2, 6.0, 6.4, and 12.8 s. We integrated the data for 5 min prior to analyzing the spectra conventionally
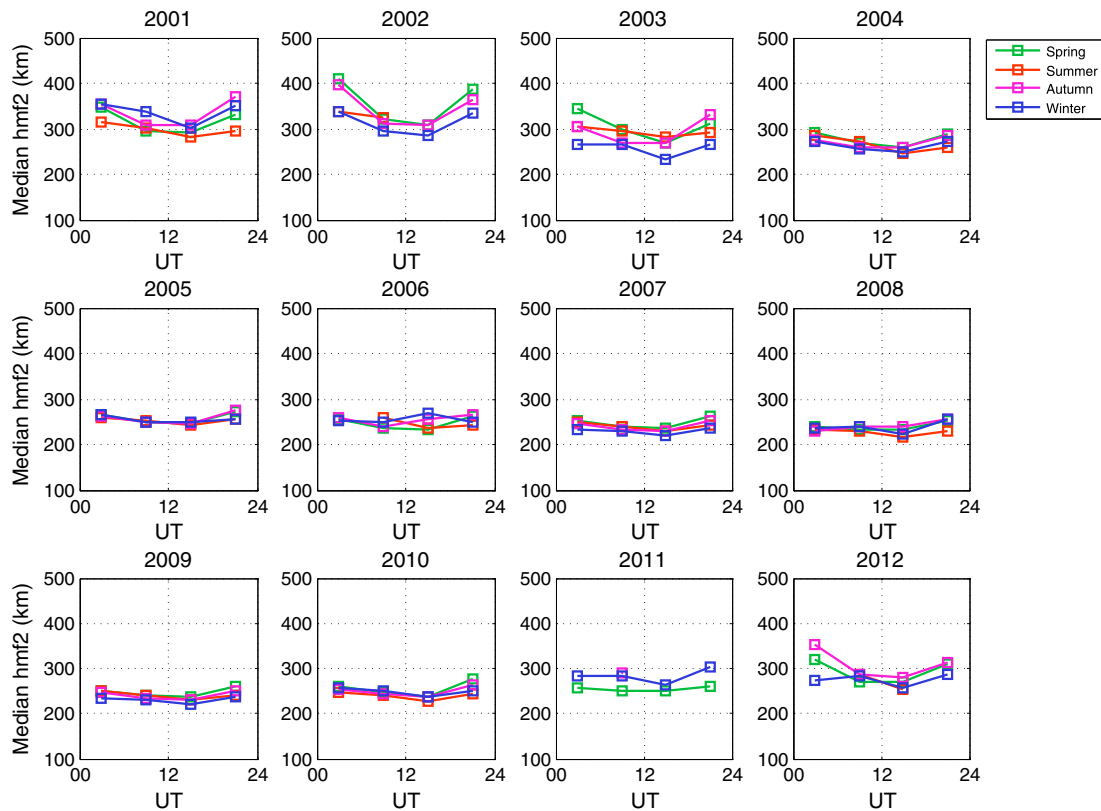
Figure 1. Variation of h_mF_2 (derived from the ESR electron density profiles) as a function of UT. Median h_mF_2 is shown for 4 UT bins (00–06, 06–12, 12–18, and 18–24 UT) for 12 full years of the ESR operations from 2001 to 2012.

using the Grand Unified Incoherent Scatter Data and Analysis Package [*Lehtinen and Huuskonen*, 1996]. The analyzed data provide the input plasma parameters to the software which allows atomic oxygen density estimates to be made from the simplified ion momentum equation. A thorough description of the procedure for the derivation of the atomic oxygen density estimates is given in *Vickers et al.* [2013].

The simplified ion momentum equation is valid for topside ionospheric altitudes. However, the height of the F layer peak (h_mF_2) can vary with both time of day and solar activity. We have therefore investigated the variation of the F layer peak height for our data set as a function of universal time. We have done this in order to determine when and at what altitude the topside condition is always fulfilled. We derived an approximate estimate for the peak height from electron density data in the following way. First, the range gate where the density maximizes was identified. We then fitted a second-order polynomial to five data points around the peak, that is to say two range gates above and below the altitude where peak was identified. We found this number of range gates to be ideal for facilitating the polynomial fitting procedure. The height where the fitted polynomial maximized was taken as an estimate for h_mF_2. A lower and upper limit on the altitude range we searched was set at 180 and 600 km, respectively. In order to eliminate erroneous electron density profiles we set a number of filtering criteria on the profiles. Data where the uncertainty in the electron density at the peak that exceeded 50% were excluded, as were profiles where the distance between the maximum density and the second highest density value was greater than five range gates. The heights derived from this method were then grouped into four bins in universal time and four season bins each of 3 months (spring, February–April; summer, May–July; autumn, August–October; and winter, November–January), and a median value for each bin was obtained. We used four bins in UT: 0–6 UT, 6–12 UT, 12–18 UT, and 18–24 UT. The variation of the F layer peak height is illustrated as a function of UT and season for each year in Figure 1. Here it becomes clear that the greatest diurnal variation is observed during the years of higher solar activity in 2001–2002. Typically, the height can reach up to 400 km during nighttime hours under these conditions while the highest daytime altitude for these solar maximum years is around 325 km.

An additional altitude limitation arises due to declining signal-to-noise ratio (SNR) of the radar with altitude. *Vickers et al.* [2013] found that during the IPY (solar minimum), an upper limit of approximately 400 km was set on the height where the atomic oxygen density estimates could be made due to this SNR limitation. The lower limit of the IPY study at 250 km was close to the *F* region peak where the plasma pressure gradient can become very small and/or variable. Since the atomic oxygen density estimates are proportional to this pressure gradient, the variability of the estimates at this altitude were deduced to be the main reason that the method was less effective at 250 km than at 350 km. Using this technique, the atomic oxygen density variation can only be studied for a fixed altitude in the range 350–400 km at the ESR. For the purpose of this study we concentrate on the results for 350 km, which is far enough from the *F* region peak during solar maximum but not too far in range that the SNR becomes poor at solar minimum and within the CHAMP orbital altitude. Based on the findings described above, we selected only the atomic oxygen density estimates corresponding to the 06–18 UT daytime interval. These estimates were subsequently grouped according to month and year.

The present study differs slightly from the earlier IPY study of *Vickers et al.* [2013] in that we have not further binned the data according to the level of magnetic perturbation. This additional step was applied to the ESR IPY data in order to extract an estimate of the atomic oxygen density for zero geomagnetic activity. The method was feasible using the IPY data set since the ESR ran near-continuously for an entire year, and therefore, bin statistics were satisfactory. In this study, we found an insufficient number of data samples within each month bin to carry out successful binning using magnetometer measurements and have therefore not carried out this step to obtain our monthly median estimates.

2.2. CHAMP Satellite

Accelerometer measurements of satellite drag made on board the polar-orbiting low-altitude CHAMP satellite are used to provide estimates of the in situ total mass density. The CHAMP satellite [*Reigber et al.*, 2002] was launched on 15 July 2000 into a high-inclination orbit of 87.3° at an altitude of approximately 450 km. Over the course of the CHAMP mission, which ended on 19 September 2010, the orbital altitude declined from its initial height of 450 km to a little under 300 km. A set of CHAMP-ESR conjunctions were identified throughout the 10 year mission were obtained using the Satellite Situation Centre spacecraft locator tool (SSCWeb). We identified conjunctions as instances when the CHAMP spacecraft coordinates were within ±1° of the ESR geographic latitude and longitude, i.e., 77.1–79.1°N and 15.0–17.0°E. Of the ~350 CHAMP passes that were identified to meet these criteria, only 17 occurred during an interval of $Kp \leq 2$ where the ESR estimates of the neutral density were also available. The ESR estimates made during the IPY alone account for 10 conjunctions. The substantial reduction results from fewer experiments during the non-IPY years. An overview of dates and times of the conjunctions are shown in Table A1 in the Appendix.

The STAR accelerometer instrument on board CHAMP measures the sum of all the forces on the satellite surface. The reader is referred to *Sutton et al.* [2005] and *Sutton* [2009] for a full description of the force model used in the STAR accelerometer data processing and estimation of the total mass density. The time resolution of the CHAMP data used was 10 s, which corresponds to a spatial separation of approximately 80 km between consecutive measurements along the satellite track. Since the orbital altitude of CHAMP was not constant but rather declined over the course of the time interval of interest, we use the mass density measurements made at the satellite altitude. We then determine the ESR range gate which falls as close as possible to the satellite altitude. Our ESR estimates are made at range gate heights that are typically separated by 20–25 km. For the purpose of comparing both the ESR and CHAMP measurements, we have converted the CHAMP total mass density into an equivalent atomic oxygen number density by dividing the measurements by the atomic oxygen mass.

3. Analysis and Results

3.1. Solar Cycle Variation of Atomic Oxygen Density at 350 km

The resulting time series for the ESR estimates of the atomic oxygen density at 350 km are illustrated in Figure 2a. The time series is constructed by taking the median value over each month for the entire 13 year period. We illustrate also the time series corresponding to MSIS data which have been obtained for the same times as we have ESR estimates. The uncertainties in the monthly median values for both the ESR and MSIS estimates were computed using a bootstrap method with 1000 iterations. It can be seen that there is
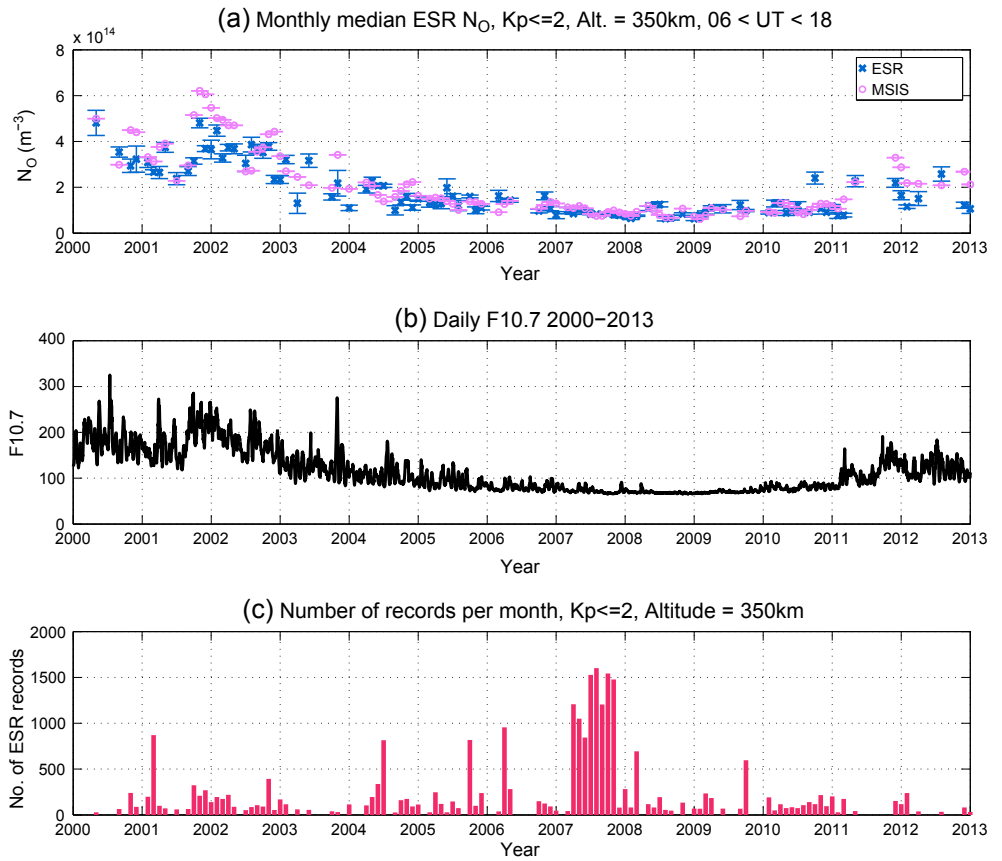
Figure 2. (a) Time series of the monthly median thermospheric density at 350 km estimated using the ESR 42 m dish data (blue) and from MSIS (lilac) from 2000 to 2012, (b) time series of the $F_{10.7}$ index from 2000 to 2012, and (c) distribution of the number of the ESR samples over all months. Only months where the sample number exceeded the threshold of 25 are shown.

roughly a factor of 5 to 6 reduction in the atomic oxygen density between typical values at solar maximum of 4–$5 \times 10^{14}\,\mathrm{m^{-3}}$ in 2002 and the lowest values reached during solar minimum. These were of the order $8 \times 10^{13}\,\mathrm{m^{-3}}$ by the beginning of 2008. Figure 2b shows the time series of the solar activity index $F_{10.7}$. We see from Figures 2a and 2b that the thermospheric density at 350 km follows the variation in the solar activity index $F_{10.7}$. $F_{10.7}$ decreases by roughly a factor of 4 from a maximum of around 250 solar flux units (sfu) in early 2002 to 60–70 sfu in 2008. We see also in Figure 2a that by the end of the period in December 2012, there are indications of an increase in thermospheric density which follow the recovery in solar activity. It is clear that the maximum values of $F_{10.7}$ corresponding to the current solar maximum are lower than those at the maximum of the previous solar cycle. However, the thermospheric density appears to be less than half the highest values reached in the beginning of 2002.

Figure 2c shows the number of samples per month bin which contributed to the median. There are a number of months where we lack any ESR estimates during the 13 year interval. We set a threshold count of 25, 5 min samples for calculating the median density for a particular month. Figure 2c illustrates only the months where the number of samples available exceeded this threshold. In total there were 52 months where we did not calculate a median. The near-continuous operations of the IPY are immediately obvious and account for 44% of the total number of estimates made over the 13 year period while the years 2000, 2003, 2011, and 2012 appear to be especially lacking in data.

3.2. Parameterization of the $F_{10.7}$ Dependence

Earlier studies that have attempted to quantify the dependence of the thermospheric density on the level of solar flux have used both the daily $F_{10.7}$ index and also the composite index $P10.7 = 0.5\left(F10.7 + \overline{F10.7_{81}}\right)$, where $\overline{F10.7_{81}}$ is the 81 day average $F_{10.7}$ [*Guo et al.*, 2007; *Liu et al.*, 2005; *Müller et al.*, 2009]. In both cases it has
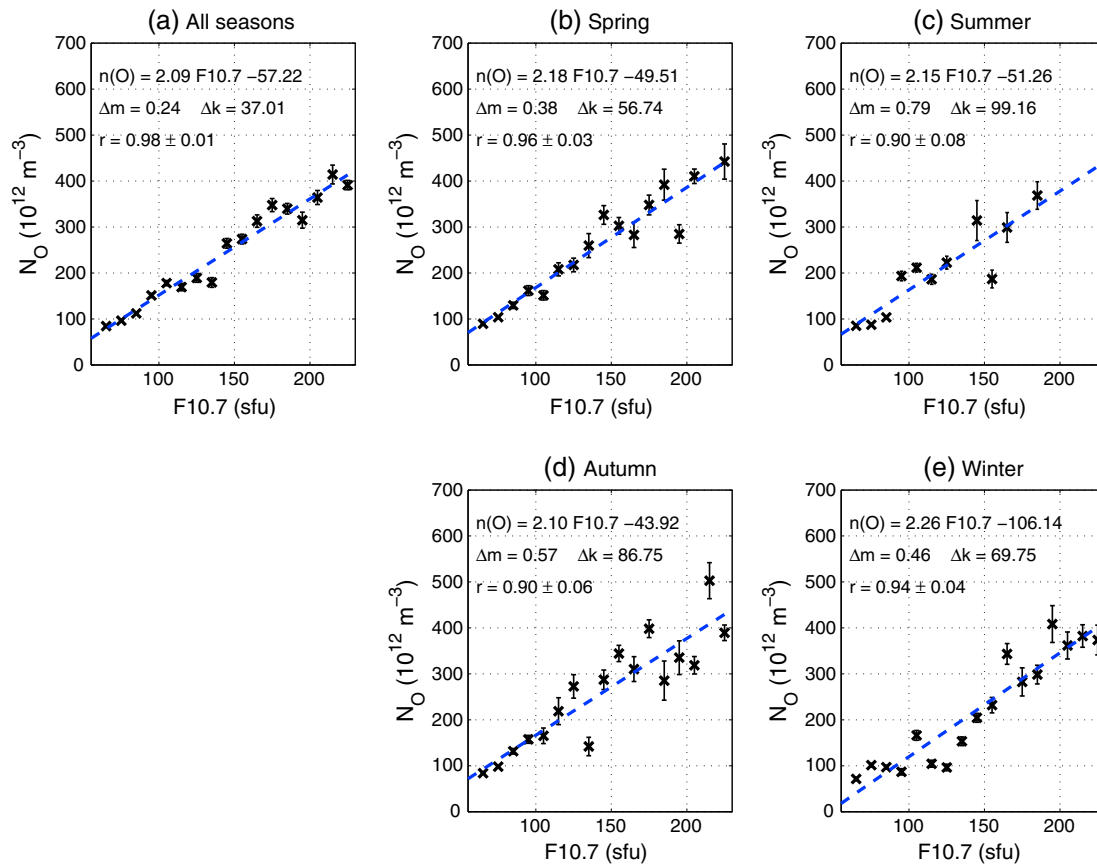
Figure 3. The ESR atomic oxygen density estimates binned in $F_{10.7}$. The median density in each bin are plotted. Bin values indicate the middle of the bin. Linear fit to bins with sample count >25 is stated with the uncertainty in the fitted slope and constant term Δm and Δk and correlation coefficient r for (a) all the ESR estimates, (b) estimates from spring months only (February–April), (c) summer months (May–July) only, (d) autumn months (August–October), and (e) for winter months (November–January).

been found that a linear function describes reasonably well the dependence, and we thus make the same assumption for our analysis by using the $F_{10.7}$ index to parameterize the atomic oxygen density at 350 km. To our knowledge, only one study has reported on the dependence of the upper thermospheric density on solar activity at high latitudes [*Liu et al.*, 2005], but it is not clear whether their results applies to the thermosphere inside the polar cap.

Our parameterization was carried out by taking all the ESR estimates from the 13 year data set and binning the samples according to the daily noontime $F_{10.7}$ values associated with the day of year and year of the ESR estimate. Eighteen bins in $F_{10.7}$ ranging from 50 to 230 sfu in steps of 10 sfu were used. The median of each bin was calculated, and the uncertainty of the medians was estimated using a bootstrap method comprising of 1000 iterations. A linear fit was then obtained by regression analysis, and we use the fitted linear function as a means of deducing the dependence of the atomic oxygen densities on the level of solar activity. Figure 3a shows the results of this fitting to the $F_{10.7}$ index with the fitted function and correlation coefficient indicated at the upper edge of the figure. We see from Figure 3a that the linear fit to the whole data set is rather satisfactory with a correlation coefficient r of 0.98 ± 0.01.

We have subsequently chosen to investigate whether seasonal variations exist in the solar activity dependence. This was done by categorizing all the 5 min samples into four seasons and binning the data in $F_{10.7}$. We have then calculated the median values for each $F_{10.7}$ bin and performed the linear fit. In performing the linear fit we have not constrained the constant term of the linear model to be positive. We only obtain the best fit to the range of $F_{10.7}$ for which we have density estimates for, and this is limited to a minimum $F_{10.7}$ of approximately 50 sfu. We consider this to be reasonable in keeping with earlier published results [e.g., *Liu et al.*, 2005; *Müller et al.*, 2009]. Our four season categories follow those which were used to study the F layer peak
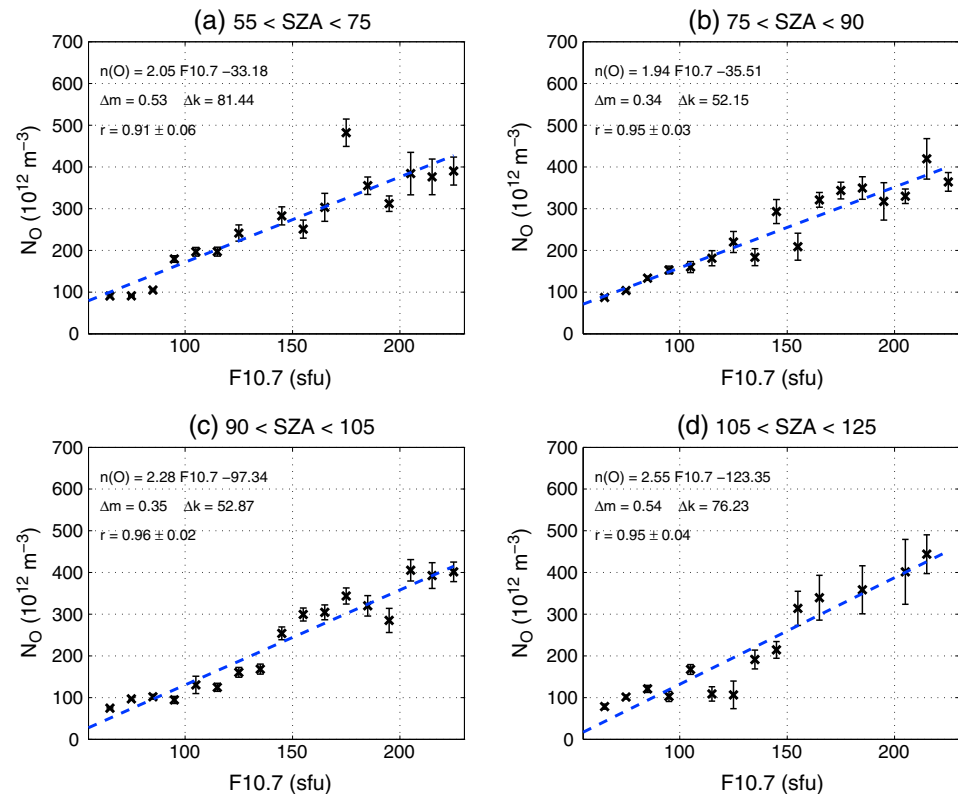
Figure 4. ESR atomic oxygen density at 350 km binned by $F_{10.7}$ and solar zenith angle (SZA). The median density at the middle point of each $F_{10.7}$ bin are plotted, where the sample count was >25 is shown for four bins in SZA (a) 55–75°, (b) 75–90°, (c) 90–105°, and (d) 105–125°; Δm, Δk, and r are again the uncertainty in the fitted slope and constant term and correlation coefficient, respectively.

height as described in section 2.1. Figures 3b to 3e show how the dependence of the atomic oxygen density on $F_{10.7}$ varies with season. We see that while the dependence of the atomic oxygen densities on solar activity in the winter months (Figure 3e) is somewhat greater than during the other three seasons, the difference between the slope for winter ($2.26 \pm 0.46 \times 10^{12}$) and the slopes of the linear fits for spring ($2.18 \pm 0.38 \times 10^{12}$), summer ($2.15 \pm 0.79 \times 10^{12}$), and autumn ($2.10 \pm 0.57 \times 10^{12}$) is nevertheless smaller than the uncertainty in the slopes (indicated as Δm in the figure panels) at the 95% confidence level. The correlation coefficients for all seasons are reasonably high, ranging from $r = 0.90 \pm 0.08$ for the summer months, $r = 0.90 \pm 0.06$ in the autumn months, to $r = 0.94 \pm 0.04$ for the winter months, and $r = 0.96 \pm 0.03$ in spring. The difference between the correlation coefficients for the different seasons is therefore within the uncertainty of the correlation coefficients, and we therefore cannot distinguish whether one season exhibits better correlation with $F_{10.7}$ than another.

Seasonal variations of the thermospheric density are driven by variations in solar EUV over the course of the year. To isolate variations in EUV over the course of a day, we employ the solar zenith angle (SZA) calculated at the altitude of the observations. We use four bins in SZA: 55–75°, 75–90°, 90–105°, and 105–125°. When the data are further binned by $F_{10.7}$ (in steps of 10 sfu from 50 to 230) and linear regression is performed to the median values, we obtain the results as shown in Figures 4a to 4d for each level of SZA. The results show a slightly increased dependence of the atomic oxygen densities on solar activity when SZA increases. However, we note again that the largest difference between the fitted slopes for the different SZA bins, typically $0.5 \times 10^{12} \, \mathrm{m}^{-3}$ is of the order of the uncertainty in the fitted slope Δm at the 95% confidence level, which ranges from 0.3 to $0.5 \times 10^{12} \, \mathrm{m}^{-3}$. Therefore, the variation in the strength of the dependence of the atomic oxygen density on $F_{10.7}$ at different values of SZA is not statistically significant. Overall, binning the atomic oxygen densities by SZA produces similar levels of correlation with $F_{10.7}$ when comparing with the results obtained from binning by season.
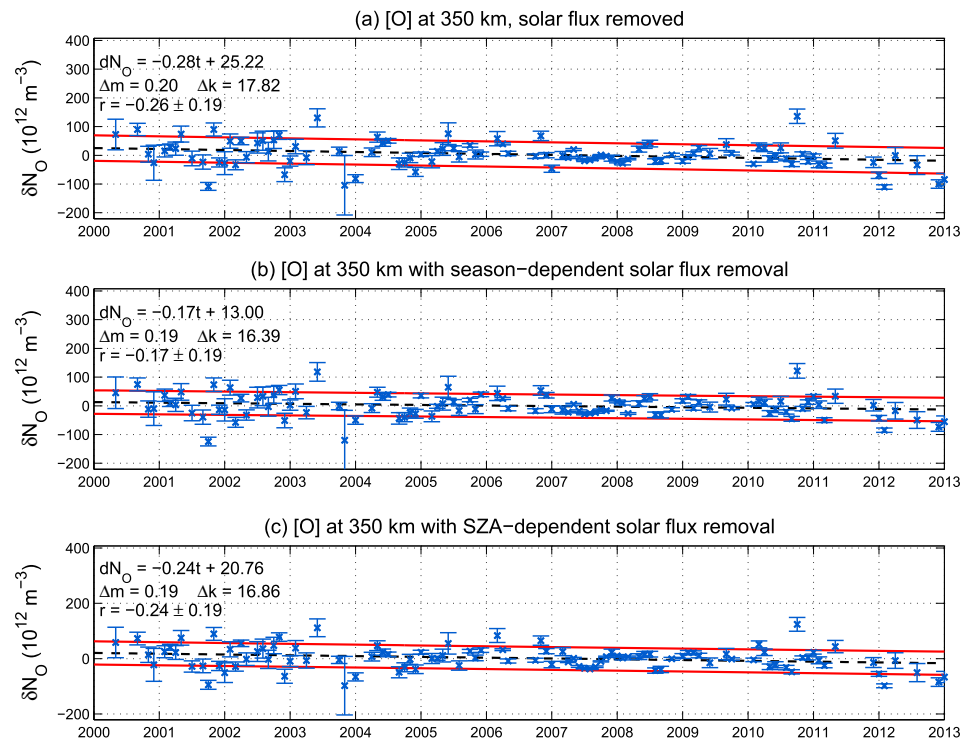
Figure 5. (a) Monthly median residual density after subtraction of the solar activity effect, calculated using the linear fit shown in Figure 3a, (b) same as Figure 5a but using the linear fits obtained by season binning, (c) same as Figure 5a but using the linear fits obtained by SZA binning. Uncertainties in the slope and constant term of the linear fits are Δm and Δk, and r is the correlation coefficient. Error bounds of the linear fit are indicated by the solid red lines.

3.3. Removal of the Solar Activity Dependence

We employ the linear fits that were made in section 3.1 in order to adjust the atomic oxygen density estimates according to solar activity associated with each estimate. This stage of the study is of interest since we wish to eliminate the solar activity influence and examine whether or not there exists an underlying trend in the atomic oxygen density over the 13 year time span which is not attributed to the solar cycle. Geomagnetic activity variation in the density values has been accounted for through the selection of data only corresponding to $Kp \leq 2$.

Hereafter, we refer to a value calculated from the linear fit to $F_{10.7}$ as the "model" value. For each estimate of atomic oxygen density, a model value is calculated according to the daily noontime $F_{10.7}$ index corresponding to the day of year and year of the estimate. We then subtract the model value from the ESR estimate to obtain a residual density. Once we have subtracted the solar activity effect from all estimates in the 13 year data set, we group the samples according to month and year and take a median of the residual densities over each month. Figure 5a shows the monthly medians of the residual densities as calculated by subtracting the model densities from the ESR estimates when no seasonal considerations are made. The time series shown in Figure 5b corresponds to the monthly median of the residual densities which are obtained using the different season dependencies of the atomic oxygen density on the $F_{10.7}$ index as shown in Figures 3b to 3e. For comparison, we have also included in Figure 5c the time series of the monthly median residual densities which are calculated from the $F_{10.7}$ dependencies obtained through binning the ESR estimates by SZA value.

If the behavior of the upper thermosphere above the ESR is consistent with the average global behavior as observed using satellite measurements, we may expect an overall decline in the atomic oxygen density residuals resulting from some other driver than solar activity. A decadal-scale decline may reflect the secular changes in global thermospheric density that have possible links to increased carbon dioxide concentrations in the lower atmosphere. To address this possibility, we have performed a linear
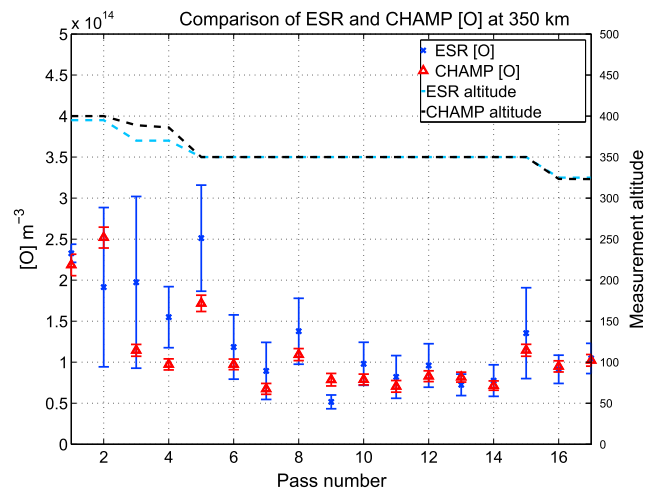
Figure 6. Comparison of the CHAMP and ESR density estimates for 17 conjunctions identified between 2001 and 2009. The orbital altitude of CHAMP (black dashed line) and the closest ESR range gate (blue dashed line) are indicated together with the CHAMP (red triangle) and ESR (blue cross) measurements at the respective altitudes.

regression to the density residuals and the fit is described by the equations stated in the upper left hand corners of Figures 5a–5c. These are discussed in section 4.

3.4. CHAMP Conjunctions

We present in Figure 6 an overview of the 17 CHAMP and the ESR estimates for the atomic oxygen density. For each conjunction identified, we take the mean value of all the ESR 5 min estimates made within the same hour of the conjunction and calculate their error bars. We show also the height of the CHAMP satellite for each conjunction and the range gate at which the ESR estimates are made at. For passes 3 and 4, the altitudes of the CHAMP and the ESR estimates differ most but are still within a scale height of each other. For the remaining 15 passes, the altitudes of both CHAMP and the ESR agree well.

In the overview are included also 10 comparisons made during the IPY between March 2007 and February 2008, and these results have been published elsewhere [*Vickers et al.*, 2013]. Although the agreement between CHAMP and the ESR for passes 2 to 5 is generally not as good as those made later during the CHAMP mission, the CHAMP measurements do tend to fall within the error bars of the ESR estimates. We note that the ESR estimates for passes 3 to 5 are typically of the order 1.5 times the CHAMP measurement, while for pass 2 the ESR estimate is 25% smaller than the CHAMP measurement. With the exception of pass 9, the difference between the two measurements is smaller for the remaining passes. Typically, the ESR estimates are 10 to 20% greater than CHAMP and in very good agreement (to within a few percent) for the last two passes from 2009 (passes 16 and 17). We also draw attention to a correction which has been made to the CHAMP measurement shown for pass 9. An earlier figure of 11.09×10^{13} m^{-3} was published in the IPY study of *Vickers et al.* [2013] and corresponded to the only case (pass 4) where the CHAMP measurement did not fall within the error bars of the ESR estimate. However, we have since identified that this measurement corresponded to an incorrect time. We therefore show the CHAMP density measurement for the correct time of the conjunction. This shows that despite the correction, the earlier ESR estimate still lies outside of the error bars of the updated CHAMP measurement.

Approximately one quarter (4 passes) of the comparisons show that the ESR density is less than CHAMP while the remaining 13 passes show that the ESR estimates exceed those of CHAMP. However, the occurrences where the ESR density is less than CHAMP are not found to occur at any single stage of the mission or at any particular time of day. The agreement between the ESR and CHAMP tends to be better during the lower solar activity years, but the sign of the difference does not exhibit any obvious dependence on solar activity or time of day. The dates and times of the conjunctions together with the percentage difference between the two measurements is summarized in Table A1 in the Appendix.

4. Discussion

This study has drawn on a recently developed method for estimating the upper thermospheric density above the EISCAT Svalbard radar. We have shown that the technique can be applied to a data set of incoherent scatter measurements spanning a decade and used to examine the solar cycle influence on the atomic oxygen density at 350 km, albeit with constraints on the UT which were necessary to ensure that data were taken from topside altitudes only. We find an overall reduction of a factor 5 to 6 between the solar maximum conditions of 2001–2002 and solar minimum in 2008. Satellite studies have shown that

globally, the thermospheric mass density at 400 km can vary by an order of magnitude between solar minimum and maximum [*Emmert et al.*, 2010].

We find that the $F_{10.7}$ index correlates very well with the atomic oxygen number density estimated using the ESR at 350 km when the monthly median values are considered. This contrasts somewhat with earlier results which report on poor correlation between the two variables at high latitudes [*Liu et al.*, 2005]. However, these authors found a linear dependence of the total mass density at 400 km derived from CHAMP measurements, which were made during the solar maximum year of 2002 using data from low latitudes only (30°N–30°S), $Kp \leq 2$ and daytime conditions. Seasonal differences were not reported on in this study. Their fitted linear function was described by the relationship $\rho = (0.08\, F_{10.7} - 5.31) \times 10^{-12}\, \mathrm{kg\, m^{-3}}$. If this mass density was assumed to be entirely due to atomic oxygen, which is a reasonable assumption at 400 km, then the equivalent number density dependence would be given by $[O] \approx (2.99\, F_{10.7} - 199) \times 10^{12}\, \mathrm{m^{-3}}$. Comparing this with our fitted function shown in Figure 3a, $[O] = (2.09 \pm 0.24\, F_{10.7} - 57.22 \pm 37.01) \times 10^{12}\, \mathrm{m^{-3}}$, we find that the gradient of the function derived in the present work is some 30% weaker than current published values, and even when the uncertainty in the gradient is accounted for, an upper value on our gradient of $\sim 2.3 \times 10^{12}\, \mathrm{m^{-3}}$ is still around 25% weaker. We note that our data set corresponds to monthly median densities for a 13 year data set, whereas that of *Liu et al.* [2005] considers measurements at a slightly higher altitude for 1 year of low-latitude data recorded over a more limited range of $F_{10.7}$. In another study using CHAMP data recorded between 2002 and 2005, *Müller et al.* [2009] obtained a near-identical result to *Liu et al.* [2005] using the $P_{10.7}$ index. Their fitted linear function to daytime measurements of the total mass density corresponding to 10.30–16.30 LT was given by $\rho = (0.078\, P_{10.7} - 4.722) \times 10^{-12}\, \mathrm{kg\, m^{-3}}$ which applies to data from low latitudes.

Our parameterization of the $F_{10.7}$ dependence of the thermospheric density at 350 km reveals that there exist negligible differences in the $F_{10.7}$ dependence of the thermospheric density between the four seasons. Figures 3b to 3e show that the slope of the regression line is only marginally greater during the winter months, but the difference between the slopes for the four seasons is smaller than the uncertainty in the fitted slope values at the 95% confidence level, therefore rendering the difference to be not statistically significant.

The seasonal variation of the thermospheric mass density at ~ 400 km and the physical mechanisms for its existence have been quite widely studied through both space-borne observations and modeling. Annual [*Paetzold and Zschörner*, 1961] and semiannual variations of the thermospheric mass density are generally understood to consist of a density maxima at equinox and minima in January and July. Studies that have concentrated on identifying the characteristics and physical mechanisms for the existence of the seasonal variation in thermospheric mass density are reported elsewhere [e.g., *Fuller-Rowell*, 1998; *Lei et al.*, 2012; *Qian et al.*, 2009]. It is known that the thermospheric mass density at least at middle and low latitudes reaches a maximum at March and October equinox and a minimum in the summer and winter months. Using our regression fits on the other hand would tend to suggest that the thermospheric number density at 350 km above the ESR is of comparable magnitude at all times during the year, at least for high solar activity. To illustrate this point, we see that for $F_{10.7} = 200$, the thermospheric density is ~ 3.8–$3.9 \times 10^{14}\, \mathrm{m^{-3}}$ in all seasons, being only marginally higher in spring.

The amplitude and phase of the yearly minimum-to-maximum variation in thermospheric mass density is thought to be controlled by solar activity and has been observed to be greater for higher solar activity [*Bowman et al.*, 2008; *Emmert and Picone*, 2010; *Lei et al.*, 2012; *Liu et al.*, 2013]. For $F_{10.7} \approx 100$, however, our results show that the thermospheric number density above the ESR is almost the same for spring, summer, and autumn ($\sim 1.6 \times 10^{14}\, \mathrm{m^{-3}}$), and slightly lower in winter ($\sim 1.1 \times 10^{14}\, \mathrm{m^{-3}}$). This would suggest that when considering the amplitude of the seasonal variation with respect to the actual number densities, the variation is more noticeable at low solar activity than at high solar activity. We have assumed here that this would be the case for a constant level of $F_{10.7}$ throughout the year which is more likely to be true only for low solar activity. Indeed, Figure 2b shows that during the higher solar activity years there was greater variability in the $F_{10.7}$ index and could vary from as little as 100 up to 250 sfu during the years 2000 to 2003.

We have attempted to account for both seasonal and diurnal variations by using the solar zenith angle as a bin parameter instead of only season. We see from Figures 4a to 4d that as SZA is increased from smaller to larger values, the density at 350 km increases marginally faster with $F_{10.7}$. However, as with the results of the

season binning, when one takes into account the uncertainty in the slope of the fitted function, typically of the order $\pm 20\%$ for all SZA bins, we note that the slightly higher gradient at the largest SZA bin is not significant.

The monthly median density residuals shown in Figures 5a to 5c represent the difference between the ESR atomic oxygen density estimates and the density obtained from the linear fits to the $F_{10.7}$-binned values for the cases when there is (a) no other binning except for $F_{10.7}$, (b) binning by season and $F_{10.7}$, and (c) binning in SZA and $F_{10.7}$. There is an apparent small reduction in scatter about the trend line when either seasonal or SZA effects are accounted for (Figures 5b and 5c). The regression line which is fitted to the time series of the density residuals has a negative slope in all cases, which is suggestive of an overall decrease in density between the start and end of the time period under study. For the case where we have subtracted the model value of the solar activity effect without seasonal considerations (Figure 5a), the linear fit to the density residual (δN) is given by $\delta N = \{(-0.28 \pm 0.20)t + (25.22 \pm 17.82)\} \times 10^{12}$ m^{-3} where t is the number of months starting from January 2000. The correlation coefficient $r = -0.26 \pm 0.19$ is weak with an uncertainty almost as great as the coefficient itself. When the seasonal variations of $F_{10.7}$ dependency have been used to calculate a model value, the linear fit to the density residuals becomes $\delta N = \{(-0.17 \pm 0.19)t + (13.00 \pm 16.39)\} \times 10^{12}$ m^{-3}. The slope for the season-adjusted density residuals (Figure 5b) is therefore approximately half compared to when no season differences are considered (Figure 5a). In the final case where the data are binned by SZA instead of season, we find that the regression line of the density residuals is given by $\delta N = \{(-0.24 \pm 0.19)t + (20.76 \pm 16.86)\} \times 10^{12}$ m^{-3} which is indicative of a similar decrease over the time period when compared to the density residuals obtained with and without season binning. However, in all cases the uncertainty in the fitted slope, constant, and correlation coefficient (indicated in Figures 5a to 5c) is of comparable magnitude to the actual values of the fitted parameters, if not greater.

The overall change in the density residuals over 13 years, which is of the order $\approx -2.6 \times 10^{13}$ m^{-3} using the linear fit to the season-adjusted density residuals, is equivalent to $\approx 5\%$ of the typical densities measured at solar maximum, which reached a peak of $\approx 5 \times 10^{14}$ m^{-3} in 2000. The change computed using the regression fits to the density residuals obtained from SZA binning is nearly 50% greater, of the order 3.7×10^{13} m^{-3}, or approximately 7.5% of the peak solar maximum densities noted in Figure 2a. We note that the uncertainty of the regression line values in all cases is larger than the overall change in the value of the density residuals between the start and end of the period. This therefore means that the apparent reduction in density is not statistically significant. This indicates that the ESR data set is not long enough to provide a definitive result.

Current published estimates of the thermospheric mass density decrease at 400 km put a value of approximately 2% per decade on the rate of decline for solar maximum conditions [*Emmert et al.*, 2004]. While our results hint at an apparently faster decrease of the thermospheric number density in the polar cap, the large uncertainties prevent a clear conclusion at this time.

Overall, the agreement with the CHAMP measurements at 350 km is satisfactory. However, the cases where estimates were made with the ESR during the years 2004 and 2005 proved to be noticeably worse compared with case studies during the rest of the solar cycle. One possible explanation could be that the experiment pulse code and scan pattern used to obtain the ESR data in 2004 and 2005 are associated with different data quality compared with those that correspond to the "ipy" experiments which were often used from 2007 onward. Indeed, data from these ESR experiments carried out in 2004 and 2005 using the "steffe" pulse code and "cp2" scan pattern are associated with a radar efficiency which is some 20% lower and a SNR which is a factor of 8 lower than data obtained using the "ipy" pulse code and "fixed_42p" scan pattern.

5. Conclusion

The present study has utilized a 13 year data set of observations made by the EISCAT Svalbard Radar to infer estimates of the atomic oxygen density at 350 km altitude. The method of estimation is based on the ion momentum equation simplified for field-aligned motion in the topside ionosphere under quiet geomagnetic conditions. Our primary goal in applying the method to a longer data set was to study the influence of solar activity on the thermospheric density inside the polar cap. We have found that the atomic oxygen density at 350 km decreases by roughly a factor of 5 to 6 between the solar maximum of 2002 and the solar minimum in 2008. This figure is somewhat smaller than satellite observations for 400 km, which report on order-of-magnitude decreases between solar maximum and minimum.

We have shown that the effect of solar activity on the monthly median thermospheric density at 350 km can be very well described by a linear dependence on the solar proxy $F_{10.7}$. The slope of the linear fit between the monthly median density estimates and $F_{10.7}$ index varies little with season. We find that the density appears to increase only marginally more with an increase in $F_{10.7}$ for larger values of solar zenith angle, but the difference in the $F_{10.7}$ dependence for different levels of solar zenith angle is not statistically significant.

The linear relationship between thermospheric density and solar activity has been used to study whether there are underlying changes in the thermospheric density that take place over the solar cycle period. Our results are suggestive of an overall decline in the density of a few percent between the start and end of the time period (2000–2012). However, the overall decline is smaller than the uncertainty in the fitted trend line. Only by studying long-term changes over several decades will we be able to resolve this problem by incoherent scatter radar.

Lastly, conjunctions with the CHAMP satellite have been studied. Our comparisons with CHAMP observations over the solar cycle have shown generally good agreement at altitudes ranging from ~420 to 300 km.

Appendix A: ESR-CHAMP Conjunctions in Tabulated Format

In the following Table A1, the universal time (UT) indicates the time of the CHAMP measurements. CHAMP and ESR number densities assume an atomic oxygen-only composition at an altitude of 350 km. The ESR number densities are an average of all available estimates made at 5-minute resolution over the same hour in which the CHAMP measurement was made. The final column indicates the ratio of the ESR-to-CHAMP measurement.

Table A1. Overview of the Conjunctions Between the CHAMP Satellite and ESR

Pass	Date (Day of Year)	UT	CHAMP ($\times 10^{13}\,m^{-3}$)	ESR ($\times 10^{13}\,m^{-3}$)	$\frac{|ESR|}{CHAMP}$
1	18/09/01 (261)	09:28	$21.85 \pm 5.9\%$	$23.27 \pm 4.7\%$	1.07
2	18/10/02 (291)	11:13	$25.19 \pm 5.1\%$	$19.14 \pm 50.7\%$	0.76
3	22/05/04 (143)	16:18	$11.45 \pm 6.3\%$	$19.73 \pm 53.0\%$	1.72
4	12/06/04 (164)	14:19	$9.73 \pm 7.0\%$	$15.49 \pm 24.0\%$	1.59
5	20/09/05 (263)	19:25	$17.17 \pm 5.8\%$	$25.12 \pm 25.7\%$	1.46
6	13/04/07 (103)	14:48	$9.73 \pm 6.6\%$	$11.85 \pm 33.0\%$	1.22
7	03/05/07 (123)	02:51	$6.75 \pm 9.8\%$	$8.94 \pm 38.9\%$	1.32
8	05/05/07 (125)	12:53	$10.93 \pm 6.7\%$	$13.78 \pm 29.2\%$	1.26
9	15/06/07 (166)	22:43	$7.87 \pm 7.0\%$	$5.16 \pm 16.3\%$	0.66
10	18/06/07 (169)	08:44	$7.89 \pm 8.4\%$	$9.81 \pm 26.8\%$	1.24
11	28/06/07 (179)	21:38	$7.05 \pm 10.1\%$	$8.20 \pm 31.7\%$	1.16
12	01/07/07 (182)	07:39	$8.29 \pm 8.0\%$	$9.61 \pm 27.6\%$	1.15
13	12/08/07 (224)	17:27	$8.18 \pm 7.4\%$	$7.24 \pm 18.1\%$	0.89
14	17/09/07 (260)	14:11	$7.15 \pm 7.9\%$	$7.76 \pm 24.8\%$	1.09
15	30/09/07 (273)	12:54	$11.45 \pm 6.4\%$	$13.54 \pm 40.9\%$	1.18
16	18/09/09 (261)	04:43	$9.49 \pm 7.1\%$	$9.13 \pm 18.9\%$	0.96
17	23/09/09 (266)	17:51	$10.22 \pm 7.0\%$	$10.46 \pm 17.6\%$	1.02

References

Anderson, C., M. J. Kosch, M. J. Nicolls, and M. Conde (2012), Ion-neutral coupling in Earth's thermosphere, estimated from concurrent radar and optical observations above Alaska, *J. Atmos. Sol. Terr. Phys.*, 105-106, 313–324, doi:10.1016/j.jastp.2013.04.005.

Blelly, P.-L., D. Alcaydé, and A. P. van Eyken (2010), A new analysis method for determining polar ionosphere and upper atmosphere characteristics from ESR data: Illustration with IPY period, *J. Geophys. Res.*, 115, A09322, doi:10.1029/2009JA014876.

Bowman, B. R., W. K. Tobiska, and M. J. Kendra (2008), The thermospheric semiannual density response to solar EUV heating, *J. Atmos. Sol. Terr. Phys.*, 70(11–12), 1482–1496, doi:10.1016/j.jastp.2008.04.020.

Cnossen, I. (2012), Climate change in the upper atmosphere, in *Greenhouse Gases: Emission, Measurement and Management*, edited by G. Liu, InTech, Rijeka, Croatia.

Emmert, J. T., and J. M. Picone (2010), Climatology of globally averaged thermospheric mass density, *J. Geophys. Res.*, 115, A09326, doi:10.1029/2010JA015298.

Emmert, J. T., J. M. Picone, J. L. Lean and S. H. Knowles (2004), Global change in the thermosphere: Compelling evidence of a secular decrease in density, *J. Geophys. Res.*, 109, A02301, doi:10.1029/2003JA010176.

Emmert, J. T., J. M. Picone, and R. R. Meier (2008), Thermospheric global average density trends, 1967–2007, derived from orbits of 5000 near-Earth objects, *Geophys. Res. Lett.*, 35, L05101, doi:10.1029/2007GL032809.

Emmert, J. T., J. L. Lean, and J. M. Picone (2010), Record-low thermospheric density during the 2008 solar minimum, *Geophys. Res. Lett.*, 37, L12102, doi:10.1029/2010GL043671.

Fuller-Rowell, T. J. (1998), The "thermospheric spoon": A mechanism for the semiannual density variation, *J. Geophys. Res.*, *103*(A3), 3951–3956, doi:10.1029/97JA03335.

Guo, J., W. Wan, J. M. Forbes, E. Sutton, R. S. Nerem, T. N. Woods, S. Bruinsma, and L. Liu (2007), Effects of solar variability on thermosphere density from CHAMP accelerometer data, *J. Geophys. Res.*, *112*, A10308, doi:10.1029/2007JA012409.

Keating, G. M., R. H. Tolson, and M. S. Bradford (2000), Evidence of long term global decline in the Earth's thermospheric densities apparently related to anthropogenic effects, *Geophys. Res. Lett.*, *27*, 1523–1526, doi:10.1029/2000GL003771.

Kosch, M. J., Y. Ogawa, M. T. Rietveld, S. Nozawa, and R. Fujii (2010), An analysis of pump-induced artificial ionospheric ion upwelling at EISCAT, *J. Geophys. Res.*, *115*, A12317, doi:10.1029/2010JA015854.

Lehtinen, M. S., and A. Huuskonen (1996), General incoherent scatter analysis and GUISDAP, *J. Atmos. Terr. Phys.*, *58*, 435–452, doi:10.1016/0021-9169(95)00047-X.

Lei, J., T. Matsuo, X. Dou, E. Sutton, and X. Luan (2012), Annual and semiannual variations of thermospheric density: EOF analysis of CHAMP and GRACE data, *J. Geophys. Res.*, *117*, A01310, doi:10.1029/2011JA017324.

Liu, H., H. Lühr, V. Henize, and W. Köhler (2005), Global distribution of the thermospheric total mass density derived from CHAMP, *J. Geophys. Res.*, *110*, A04301, doi:10.1029/2004JA010741.

Liu, H., T. Hirano, and S. Watanabe (2013), Empirical model of the thermospheric mass density based on CHAMP satellite observation, *J. Geophys. Res. Space Physics*, *118*, 843–848, doi:10.1002/jgra.50144.

Marcos, F. A., J. O. Wise, M. J. Kendra, N. J. Grossbard, and B. R. Bowman (2005), Detection of a long-term decrease in thermospheric neutral density, *Geophys. Res. Lett.*, *32*, L04103, doi:10.1029/2004GL021269.

Mikhailov, A. V., and J. Lilensten (2004), A revised method to extract thermospheric parameters from incoherent scatter observations, *Ann. Geophys.*, *47*, 985–1008.

Müller, S., H. Lühr, and S. Rentz (2009), Solar and magnetospheric forcing of the low latitude thermospheric mass density as observed by CHAMP, *Ann. Geophys.*, *27*, 2087–2099, doi:10.5194/angeo-27-2087-2009.

Paetzold, H. K., and H. Zschörner (1961), An annual and a semiannual variation of the upper air density, *Pure Appl. Geophys.*, *48*, 85–92.

Picone, J. M., A. E. Hedin, D. P. Drob, and A. C. Aikin (2002), NRLMSISE-00 empirical model of the atmosphere: Statistical comparisons and scientific issues, *J. Geophys. Res.*, *107*(A12), 1468, doi:10.1029/2002JA009430.

Qian, L., R. G. Roble, S. C. Solomon, and T. J. Kane (2006), Calculated and observed climate change in the thermosphere, and a prediction for solar cycle 24, *Geophys. Res. Lett.*, *33*, L23705, doi:10.1029/2006GL027185.

Qian, L., S. C. Solomon, and T. J. Kane (2009), Seasonal variation of thermospheric density and composition, *J. Geophys. Res.*, *114*, A01312, doi:10.1029/2008JA013643.

Reigber, C., H. Lühr, and P. Schwintzer (2002), CHAMP mission status, *Adv. Space Res.*, *30*(2), 129–134.

Roble, R. G. (1995), Energetics of the mesosphere and thermosphere, in *The Upper Mesosphere and Lower Thermosphere: A Review of Experiment and Theory*, *Geophys. Monogr. Ser.*, vol. 87, edited by R. M. Johnson and T. L. Killeen, pp. 1–21, AGU, Washington, D. C.

Sutton, E. K. (2009), Normalized force coefficients for satellites with elongated shapes, *J. Spacecraft Rockets*, *46*(1), 112–116, doi:10.2514/1.40940.

Sutton, E. K., J. M. Forbes, and R. S. Nerem. (2005), Global thermospheric neutral density and wind response to the severe 2003 geomagnetic storms from CHAMP accelerometer data, *J. Geophys. Res.*, *110*, A09S40, doi:10.1029/2004JA010985.

Vickers, H., M. J. Kosch, E. Sutton, Y. Ogawa, and C. La Hoz (2013), Thermospheric atomic oxygen density estimates using the EISCAT Svalbard Radar, *J. Geophys. Res. Space Physics*, *118*, 1319–1330, doi:10.1002/jgra.50169.

Wannberg, G., et al. (1997), The EISCAT Svalbard Radar: A case study in modern incoherent scatter radar system design, *Radio Sci.*, *32*(6), 2283–2307, doi:10.1029/97RS01803.

Winser, K. J., A. D. Farmer, D. Rees, and A. Aruliah (1988), Ion-neutral dynamics in the high latitude ionosphere: First results from the INDI experiment, *J. Atmos. Terr. Phys.*, *50*, 369–377.